Experimental study of swirling flow characteristics in a semi cylinder vortex cooling configuration

Xiaojun Fan[a], Chuangxin He[b], Lian Gan[c,*], Liang Li[a,d,*], Changhe Du[e]

[a]*School of Energy and Power Engineering, Xi'an Jiaotong University, Xi'an 710049, China*
[b]*Key Lab of Education Ministry for Power Machinery and Engineering, School of Mechanical Engineering, Shanghai Jiao Tong University, 800 Dongchuan Road, Shanghai 200240, China*
[c]*Department of Engineering, Durham University, Durham, DH1 3LE, UK*
[d]*Shaanxi Engineering Laboratory of Turbomachinery and Power Equipment, Xi'an 710049, China*
[e]*School of Energy and Power Engineering, Northeast Electric Power University, Jilin 132012, China*

Abstract

This study utilised planar Particle Image Velocimetry (PIV) to investigate the flow characteristics in a semi cylindrical confinement with 2 jet inlets. The water based experimental study aims to understand the basic flow behaviour in a gas turbine leading edge vortex cooling configuration. The time averaged and fluctuating flow fields were collected at 3 cross sections and 1 longitudinal section at 3 different inlet Reynolds numbers. The snapshot based Proper Orthogonal Decomposition (POD) was applied to extract the coherent flow characteristics. Results showed that the vortex flow consists a large-scale vortex in the chamber with a small recirculating corner vortex. The core vortex is similar to the Rankine vortex with a near solid body rotating vortex, surrounded by a jetting vortex layer and a boundary layer along the chamber wall. The jetting vortex layer featuring a proportional decline of circumferential velocity is different to the potential layer in a typical Rankine vortex. The jetting vortex at a high velocity level is mainly responsible for the high heat transfer rate for vortex cooling. A turning region at $\theta \approx 170°$ separating the circumferential velocity behaviour was noticed, which provides a flow dynamic explanation to the heat transfer intensity along the surface wall for vortex cooling. The region at the interface between the solid body rotating vortex and the jetting vortex features with relatively low velocity magnitude but strong shear and large fluctuating velocity intensity. The longitudinal section has a low average velocity (approximately 10% of that in the cross sections in magnitude), indicating the vortex flow is strongly rotational but weakly helical. However, the fluctuating velocity intensity has a comparative level to cross sections. POD analysis reveals that the first 4 modes contain about 23.2% of the fluctuating velocity energy. In nozzle cross sections, the coherent vortex near the surface wall dominates the fluctuation energy and is responsible for the heat transfer enhancement. In the cross section between nozzles, the coherent flow structure displays a vortex pair in the core and a minor corner vortex.

Keywords: vortex cooling, flow fields, PIV, POD

1. Introduction

Vortex flows have many applications in industrial processes like combustor, hydrocyclone, separator and rotating machinery[1]. In gas turbine blade cooling, vortex flow has been used to provide a better heat protection for the blade

*corresponding author
Email addresses:* `lian.gan@durham.ac.uk` (Lian Gan), `liliang@mail.xjtu.edu.cn` (Liang Li)

leading edge[2]. This cooling method is often called vortex cooling or swirl cooling. The blade leading edge bears the direct scour of extremely hot gas at a temperature level of 1900K approximately, which is far beyond the material melting point. Thus, efficient cooling methods become imperative. While impingement cooling has been applied to the leading edge[3], Kreith and Margolis[4, 5] found that vortex flow in a pipe could enhance the heat transfer coefficient four times larger than a single impingent flow. Since then, vortex flow has attracted much attention in blade cooling applications. Considering the leading edge cooling passage in a gas turbine blade is similar to a semi cylinder and the curved surface is suitable to generated a vortex flow, recent studies of vortex cooling suggested a more efficient heat transfer potential and a better match of blade leading edge cooling passage compared to other cooling techniques in general [6, 7].

Extensive research has been carried out in terms of enhanced heat transfer induced by vortex flow. The pioneer experimental work of Hay and West[2] found that the local heat transfer was closely related to the swirl number. Based on their experiments[2], Glezer et al.[8] developed a vortex cooling method which was applied to the blade cooling system. Different cooling structures with multiple nozzles were compared to obtain the optimal configuration. Hedlund et al.[9, 10, 11] carried out a series of experiments about vortex cooling in a circular pipe, and found that temperature ratios and Reynolds number were critical parameters for cooling efficiency. Ling et al.[12] performed experimental and numerical studies, where the Transient Liquid Crystal Technology was used to observe the heat transfer coefficient. They found that heat transfer distribution resulted from vortex cooling was more uniform than other cooling methods. Liu et al.[13, 14, 15] established a cylindrical vortex cooling configuration for blade leading edge and conducted a series of numerical simulations to explore the aerodynamic and geometric influences on the cooling performance. It was found that heat transfer performance and pressure loss were sensitive to Reynolds number, jet nozzle aspect ratio and the ratio of swirl chamber radius to the jet slot height. Whilst most previous studies were based on a simple cylindrical geometry, Du et al.[16, 17, 18] proposed a semi cylinder vortex cooling passage which performed reasonably well for gas turbine blade leading edge. They also investigated the effects of nozzle geometry and aerodynamic parameter comprehensively and found that both imposed a significant effect on the cooling efficiency.

Many fundamental studies have also been conducted to understand the mechanisms of vortex flow for cooling purposes. Over the last 60 years, vortex flow in simple tube configurations was experimentally and numerically studied extensively. Nissan et al.[19] studied vortex motions in a vertical cylinder and proposed three types of velocity profiles, which were functions of the tangential velocity, the manner of decay of the tangential velocity, and the wall pressure drop. King et al.[20] studied the vortex decay rate in a tube, in which the vortex flow was generated by 2 inlet jets in tangential direction. Akiyama et al.[21] generated their vortex flow in a swirling pipe using 8 tangential inlet nozzles and the energy loss was studied specifically. Kitoh et al.[22] experimentally investigated the swirling flow in a fee-vortex-type pipe. The velocity distribution, swirl intensity, swirl decay coefficient and the wall shear stress were measured. Li and Tomita[23] experimentally studied the swirling flow in a circular pipe. The characteristics of the decay of swirl, the average dynamic, static and total pressures were explored. Hedlund et al.[11] visualised vortex flow behaviour downstream of inlet 2 which is posistioned close to the outlet, and the Gortler vortices were observed. Gupta et al.[24] performed Particle Tracking Velocimetry (PTV) and the RNG k-ε turbulence model based computational simulations to obtain the vortex flow visualisation in a

cyclone with one inlet. They found that the general flow structure was not sensitive to Reynolds number. Grundmann et al. [25] experimentally studied the helical structures in the vortex flow using Magnetic Resonance Velocimetry (MRV). The occurrence of a three-layered flow structure was observed.

Previous works confirmed significant cooling enhancement using vortex cooling in gas turbine blade leading edge. Vortex cooling has generally been based on two configurations: a tube of cylindrical shape[11], which is most widely used and a semi cylinder model proposed by Du et al. [18]. In gas turbine blade cooling, the second configuration was found to adapt better to the leading edge geometry according to Han et al.[26]. However, semi cylinder configuration has not been well studied. So far the only few available works on this configuration were performed by Reynolds Average Navier-stokes (RANS) modelings, where only the mean flow fields are captured reasonably well but not the fluctuating velocities, which are very important to understand the cooling mechanism in this configuration. No experimental study has been conducted to the best of the authors' knowledge.

This paper aims to provide a better fundamental understanding of the fluid dynamics inside a semi cylinder configuration, hence to elucidate the underlying physics pertinent to heat transfer augmentation. In particular, in this paper, the mean and the fluctuating velocity fields are quantified; coherent flow structures are extracted using snapshot based POD.

2. Experimental apparatus

The experiments were conducted in a glass water tank of size 2,400 mm(length)×900 mm(width)×800 mm(depth) as shown in Fig. 1. It is worth to mention that water is chosen as the working fluid for the vortex flow experiment, although air is usually used as the coolant in gas turbine blade cooling. The main reason is that water could achieve a Reynolds number about 15 times larger than the air at the same inlet velocity, room temperature and model geometry. Besides, the seeding quality of PIV is often better (more homogeneous) in a water-based experiment than in an air-based one, especially inside the complex shaped cavity understudy. According to similarity criterion, when the geometry and the Reynolds number similarities are both satisfied, the main feature of the flow physics should be captured even though the working fluid is not air. Therefore, the results of this study should be valid and could provide some useful references for the vortex flow in gas turbine blades cooling. The jet velocity ranges from 125 mm/s to 500 mm/s in the main pipe and the inflow was then split by the empty splitter chamber to nozzle 1 and 2 which are connected to the semi cylinder chamber as shown in Fig. 2. In an actual blade cooling system, the coolant for the leading edge is usually provided by the cooling passage in Mid-Region. The splitter chamber is functioned as a mimic of cooling passage to spontaneously distribute coolant for nozzles. Nozzle 1 and 2 are rectangular shape and of size 24 mm×8 mm and 150 mm long. The two nozzles are identical and arranged symmetrically about the inlet pipe. The length was chosen to ensure the flow to be sufficiently developed before entering the vortex chamber. A complex vortex flow forms in the vortex chamber, and then the flow exits from the outlet in the axial direction. The aspect ratio of the nozzles is 3, the hydraulic diameter of the vortex chamber is 39 mm and the length of the chamber is 200 mm.

The entire nozzle-chamber system is made of Perspex. The tank is evenly seeded with 10-μm silver-coated hollow glass spheres (Dantec, Denmark). The planar PIV was employed to quantify the flow field at a total of 4 sections including
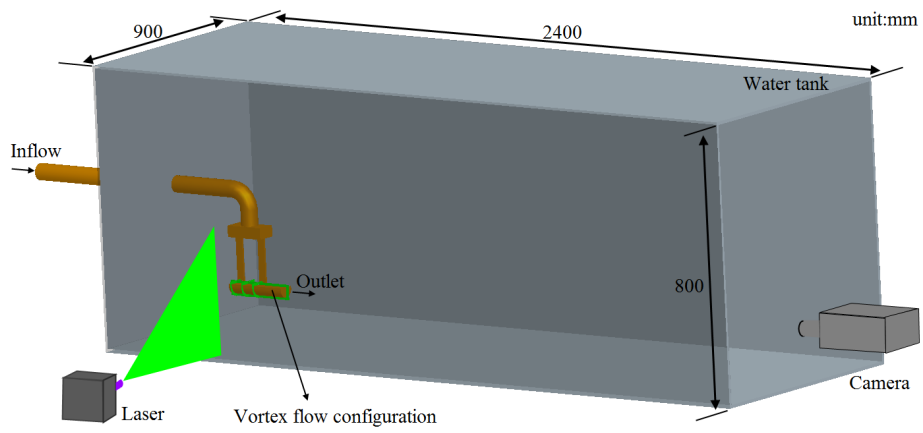
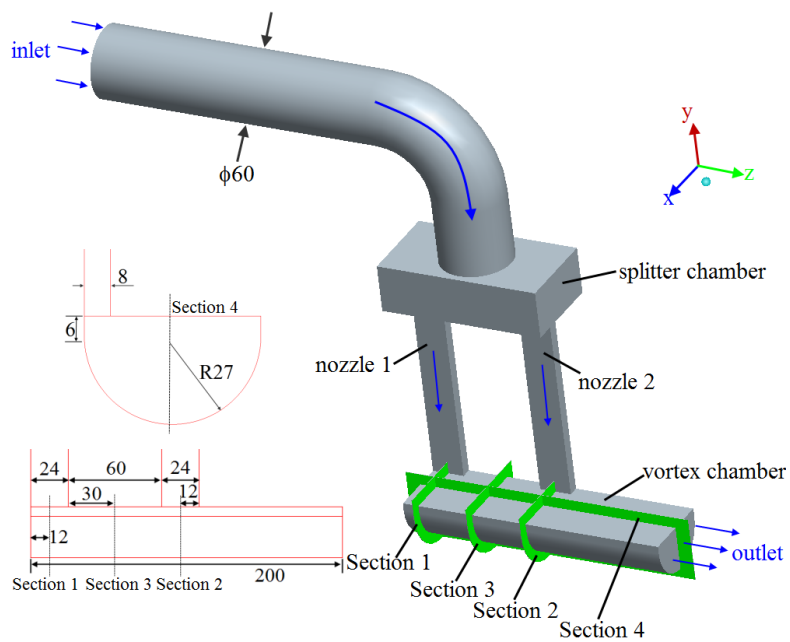Figure 1: Schematic view of the experiment setup.

Figure 2: 3D view of the vortex cooling configuration and the testing sections.

4

3 cross-sections and a longitudinal section as shown in Fig. 2. These sections were illuminated by a 532-nm Nd:YAG Laser (SoloPIV, New Wave Research) with a lens system to produce a 1-mm-thick light sheet. A 12-bit CCD camera (Sensicam, PCO, Germany) was used as the imaging tool. The imaging system was synchronised by National Instrument (BNC-2121) programmed in LabVIEW 2016 (64-bit). Three typical inlet Reynolds numbers $Re = \rho V_0 D / \mu$ = 5,000, 10,000 and 20,000 for gas turbine leading edge cooling are chosen for study. ρ, V_0, D and μ are the water density, the inflow velocity, the main pipe diameter and the water dynamic viscosity respectively. For each testing, 500 image pairs were acquired at a sample rate < 1 Hz to ensure statistical independence and sufficient convergence for the quantities presented here. For all the testing sections shown in Fig. 2, two-dimensional calibration was performed to account for the possible optical distortion. The particle images were processed by Davis 7.0 (LaVision, Germany) to obtain the flow vector fields.

3. Proper orthogonal decomposition (POD) definitions

Snap-shot based POD [27] was applied to assist the flow field analysis. It decomposes the original 500 velocity fields into a sum of weighted, linear basis functions or modes, thus to extract the coherent flow structures with the mean velocity removed. Briefly speaking, the instantaneous velocity field data $\mathbf{u}^n$ is a finite sum in the variables-separated form in Eq. 1.

$$\mathbf{u}^n = \sum_{i=1}^{N} a_i^n \phi^i = \psi \mathbf{a}^n, \tag{1}$$

$$\mathbf{a}^n = \psi^T \mathbf{u}^n, \tag{2}$$

where a_i^n are the coefficients determined by projecting the velocity onto the POD modes as shown in Eq. 2, n is the snapshot number and ϕ^i is the spatial POD mode.

The velocity matrix $\mathbf{U}$ is defined based on the experimental data as shown in Eq. 3.

$$\mathbf{U} = [\mathbf{u}^1 \mathbf{u}^2 \cdots \mathbf{u}^N] = \begin{bmatrix} u_1^1 & u_1^2 & \cdots & u_1^N \\ \vdots & \vdots & \vdots & \vdots \\ u_M^1 & u_M^2 & \cdots & u_M^N \\ v_1^1 & v_1^2 & \cdots & v_1^N \\ \vdots & \vdots & \vdots & \vdots \\ v_M^1 & v_M^2 & \cdots & v_M^N \end{bmatrix}, \tag{3}$$

where N=500 is the total number of vector fields. M is the number of grid data points in each vector field, which is 160×128 in this case. The auto-covariance matrix $\mathbf{C}$ is constructed as

$$\mathbf{C} = \mathbf{U}^T \mathbf{U}. \tag{4}$$

Applying the eigenvalue decomposition of the matrix $\mathbf{C}$ (Eq. 5), the eigenvalue λ^i and the associated eigenvector $\mathbf{A}^i$

Table 1: Nozzle jet velocity U_0 at all cross sections. U_0 for Section 3 is the average of Section 1 and 2. Unit: m/s

Re	Section 1	Section 2	Section 3
5,000	0.73	0.61	0.67
10,000	1.39	1.17	1.28
20,000	2.63	2.29	2.46

can be obtained.

$$\mathbf{CA}^i = \lambda^i \mathbf{A}^i. \tag{5}$$

Sorting the eigenvalues $\lambda^i(\lambda^1 \geq \lambda^2 \geq \cdots \geq \lambda^N)$ ranks the contribution of the modal energy of the associated flow field mode $\mathbf{A}^i$. The sum of the eigenvalues reflects the total fluctuation energy. Accordingly, the spatially filtered flow field reveals the flow coherency by the linear combination of the POD modes in the top eigenvalue rankings (taking $i \ll N$ in Eq 1), resulting in a reduced-order reconstruction that captures the largest amount of turbulent kinetic energy in the flow [28]. The POD mode ϕ^i can be calculated by Eq. 6.

$$\phi^i = \frac{\sum_{n=1}^N A_n^i \mathbf{u}^n}{\left\| \sum_{n=1}^N A_n^i \mathbf{u}^n \right\|}, \ i = 1, 2, \cdots, N. \tag{6}$$

The effect of the sample size on the POD low-order reconstruction was tested using 500 and 1,000 vector fields from the same testing case. It is found that the POD eigenvalue rankings for both datasets nearly collapse for the high energy modes; figure not shown. It reassures that the present sample size (500) is sufficient to provide statistically converged results.

4. Results and discussions

4.1. Mean flow fields

The contours of the normalised time average velocity V_{xy}/U_0 and in-plane streamlines in the cross sections (Section 1, 2 and 3) at 3 inlet Re are presented in Fig. 3. Here V_{xy} is defined as $\sqrt{\overline{U}^2 + \overline{V}^2}$, $\overline{U}, \overline{V}$ are averaged velocity components in X and Y direction, and U_0 is the inlet jet velocity through nozzles 1 and 2; see Fig. 2, which is listed in Table. 1. Note that U_0 at Section 3 without jet input is the average value of Section 1 and 2. As the jets eject to the chamber tangentially at one side of the chamber, they flush along the surface wall and maintain a high momentum to the other side, while the jet material rolls up in the chamber central area forming a large core vortex. At the location where the jet interacts with the residual flow (6 mm$< x <$14 mm, 30 mm$< y <$33 mm in Fig. 3), a small recirculating corner vortex of low velocity magnitude can be observed in Section 1, 2 and 3 with increasing size for all the Re conditions.

In a typical circular cylinder vortex cooling configuration, the shape of the core vortex is usually more circular without noticeable corner vortex [28]. In the present semi cylinder configuration, the core vortex deforms to an elliptical shape due to the constraint from the top flat wall. The corner vortex is likely to cause more loss due to the increased flow complexity and turbulence. As the inlet Re increases, the flow pattern remains roughly the same, with the exception at Section 1, where the core vortex location is slightly shifted from $Re = 5,000$ to $10,000$. It is worth mentioning that the velocity in nozzle
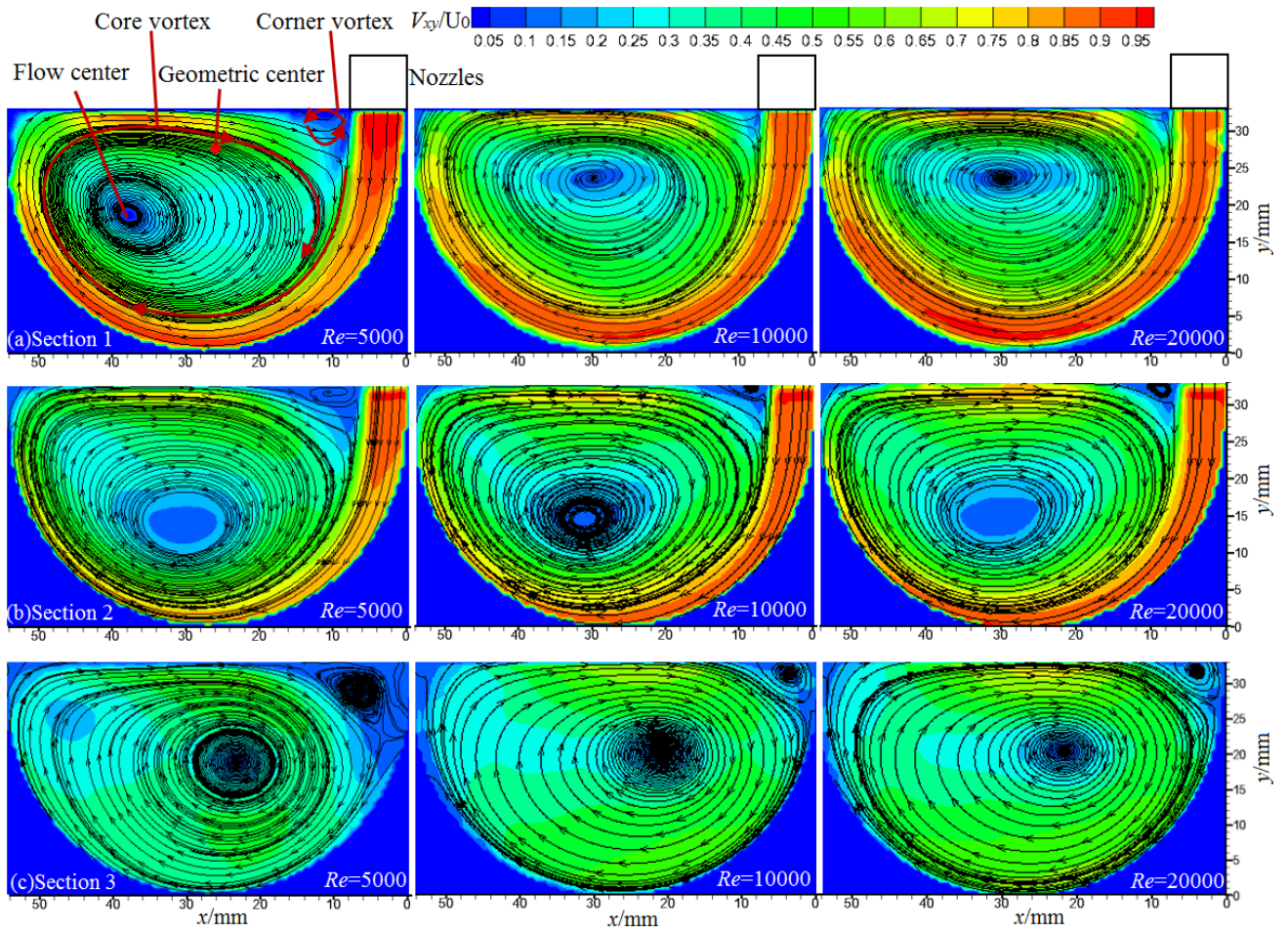
6

Figure 3: The time average velocity contour and the in-plane streamlines of cross sections at 3 inlet *Re* conditions.

2 is smaller than that in nozzle 1, which is a fluid mechanical effect consistent to our numerical study [6]. This is because of the pressure inside the chamber decreasing along the flow direction towards outlet, causing the mass flow rate in nozzle 2 smaller than that in nozzle 1. In Section 3, not surprisingly the overall velocity magnitude is lower especially at near wall regions on the other side of the corner vortex, due to lack of direct jet input. The size of corner vortex reduces with increasing Re.

For the current nozzle arrangement, the circumferential velocity is clearly the dominant component of the flow, as suggested by the streamline pattern, which is similar to the Rankine vortex [29]. This vortex typically features a solid body rotating part closer to the vortex core, where the circumferential velocity is proportional to the radius from the core centre, viz. $U_\theta \sim r$. It is surrounded by a potential vortex layer, where the circumferential velocity is inversely proportional to the radius viz. $U_\theta \sim \Gamma/r$, where Γ is the circulation of the inner solid body rotating similar to a free vortex, until the boundary layer is reached at the outer wall.

For the particular configuration studied in this paper, the circumferential velocity distribution follows a similar pattern, although the vortex is distorted by the semi cylindrical chamber. Fig. 4 presents the circumferential velocity distribution along the radial direction from the flow center to the surface wall at a chosen 30 degree in Section 1. Cases at Re =10,000 and 20,000 have a similar distribution with Biegger's model [29]. From the core center to the outer wall, velocity increases approximately linearly and reaches the peak value at $r/r_0 \approx 0.91$. This is the solid body rotating part. A small range governed by the jetting vortex relation can be seen for $0.91 < r/r_0 < 0.98$, which is further surrounded by a thin boundary layer at the chamber wall. This jetting vortex features a proportional decline of circumferential velocity. For case of Re =5,000, because of the strong interaction between the vortex and the inflow jet, the former is pushed towards the far side of the chamber as shown in Fig. 3 a. As a result, the velocity profile is deformed and is not as liner as other cases with a much lower rate when $r/r_0 < 0.7$. In all the testing cases, it is suggested that it is the jetting vortex layer which is mainly responsible for heat transfer enhancement, owing to its large velocity magnitude and geometric distribution closer to the wall. Whilst in the ideal Rankine vortex, this layer is energised by the circulation of the core solid body rotating vortex, in the current configuration, it is partly driven by the momentum of the jet directly.

The velocity distribution along the jetting vortex layer at r=23mm is further studied and presented in Fig. 5. As can be seen, the velocity magnitude in this layer increases with increasing Re, albeit normalised by the jet inflow velocity U_0, in line with Fig. 4, but the distribution pattern is similar. Probably counter intuitively, the velocity does not display a monotonically decreasing behaviour as θ increases (viz. further away from the nozzle exit) as it is shown in Section 2. In Section 1, V_{xy} gradually increases with θ until $\theta \approx 110^o$ and then decreases until $\theta \approx 170°$. The case $Re = 5,000$ is an exception, which shows a decline of V_{xy} from the nozzle exit until $\theta \approx 70^o$. As the inflow jets through narrow passages into open space, it tends to spread to both sides (z direction shown in Fig. 2). Since the nozzle 1 is positioned along the side surface wall, the spreading would be restricted and inflow would gather together. As a result, it brings a slight velocity increase for $\theta < 70^o$ in Section 1. In Section 3, without the jet supply and the existence of corner vortex, an initial increment of v with θ is also observed, with an additional plateau over $50^o \lesssim \theta \lesssim 120^o$.

According to a previous numerical study of the Nusselt number (Nu) distribution in a similar configuration as shown in
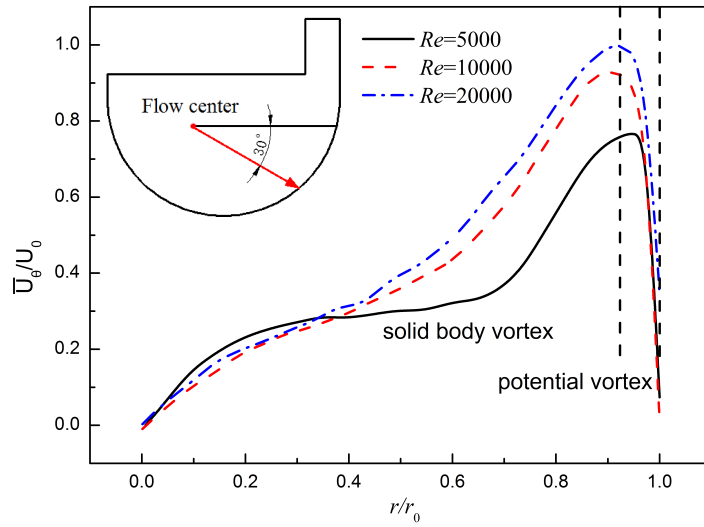
Figure 4: Circumferential velocity profile along the radial direction at 30 degrees of Section 1.
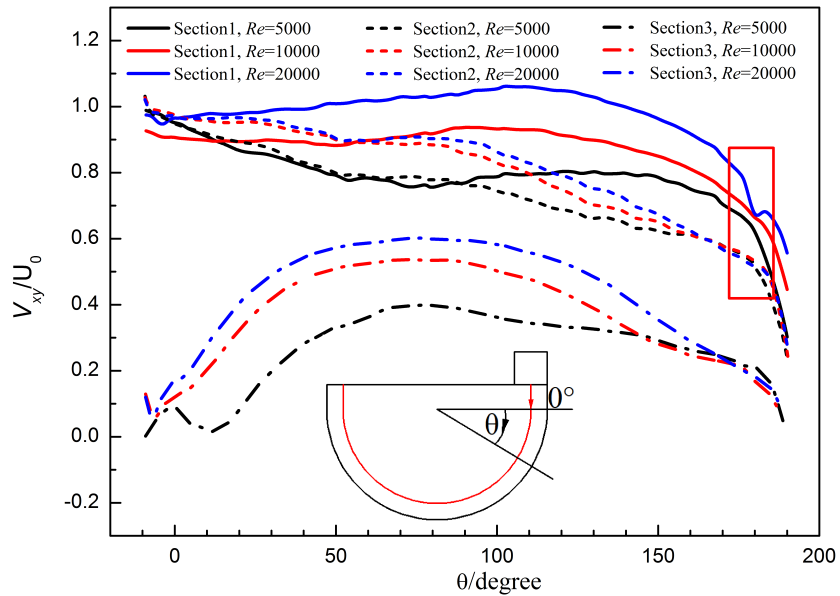

Figure 5: Normalised average velocity profile along the centre of the jetting vortex layer at r=23mm. The angle θ is defined based on the geometric center of the semi cylinder. The turning region is pointed out in the red box.

Fig. 6 [17], firstly, Nu around the nozzle exit is not uniformly distributed in a stripe-shape as one would expect. Instead, Nu along the centre of the jet trajectory is smaller than that at the two edges where strong shear occurs and decreases along the circumferential direction in a fluctuating manner. Secondly, Nu magnitude decreases quickly for $\theta > 160^o$. Considering the heat transfer intensity is closely related to the flow pattern, the velocity along the surface wall of Section 1 explains the Nu behaviour at inflow supplying regions.
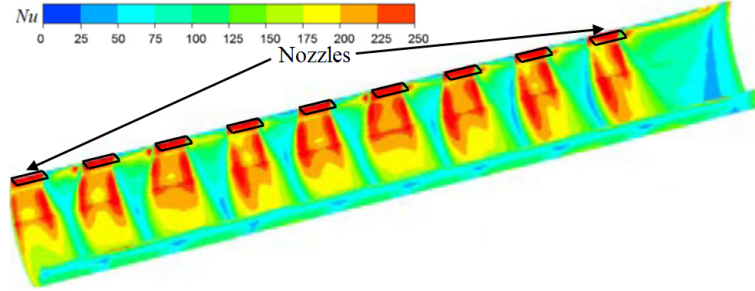

Figure 6: Nusselt number distribution of of a multiple nozzles vortex cooling configuration by Du [17].

As shown in Fig. 5, the velocity in Section 1 increases gradually along the vortex chamber wall until $\theta \approx 110°$ and then decreases slightly until $\theta \approx 170°$. This position at $\theta \approx 170°$ could be regarded as a turning region (the red box in Fig. 5) along the circumferential direction. It is an important feature of the vortex flow as well as the heat transfer distribution in such a configuration. Before the turning region, the inflow velocity maintains at a high level and a low decreasing rate, while after that region the velocity magnitude decreases dramatically fast. This is because the inflow jets along the surface wall in a typical vortex flow experiences a small flow loss until the turning region. When the inflow reaches the turning region, the geometrical structure (the top wall) blocks and deforms the vortex flow, causing the near wall flow rolls up as shown in Fig. 3. In addition, the resistance loss along the wall reduces the kinetic energy. As a result, the velocity after the turning region reduces fast while the heat transfer intensity weakened heavily.

Section 1 of $Re = 10,000$ case is chosen to present the dependence of radial velocity $\overline{U}_r$ on the radial distances from the flow centre $r = 0$ at various azimuthal angles as shown in Fig. 7. Of noted the position of flow center for each case can be slightly different. As these radial lines are normal to the local outer surface, in real heat transfer applications, $\overline{U}_r$ is responsible for taking the hot fluid at the outer radius towards the centre area of the chamber where it is relatively cold. For this particular case, and also for $Re = 20,000$ case, the flow centre is close to the geometric center. Positive velocity points outward while negative points towards the centre. At the flow center ($r \approx 0$), the $\overline{U}_r$ approaches zero not surprisingly. Closer to the surface wall ($r \approx r_0$), $\overline{U}_r$ points outward and inward at different θ angles, in line with the location of the vortex centre. As θ increases from 0° to 150°, we found $\overline{U}_r$ changes from negative velocity to positive velocity and a turning point where $\overline{U}_r$ equals zero should exit. Generally, for $\theta < 110^o$, $\overline{U}_r < 0$, which is beneficial for the inflow to take heat from the surface wall. At larger θ, $\overline{U}_r$ changes its direction gradually to point to the surface. For these areas, the cooling effect would be weakened.

Average velocity contour overlaid with streamlines in the longitudinal section 4 is presented in Fig. 8. U_0 of Section 1 listed in Tab. 1 is chosen for the reference velocity. As expected, compared to cross sections (Fig. 3), the velocity in the axial direction is small in magnitude, typically about 10%. This means that the flow in the chamber is strongly rotational,
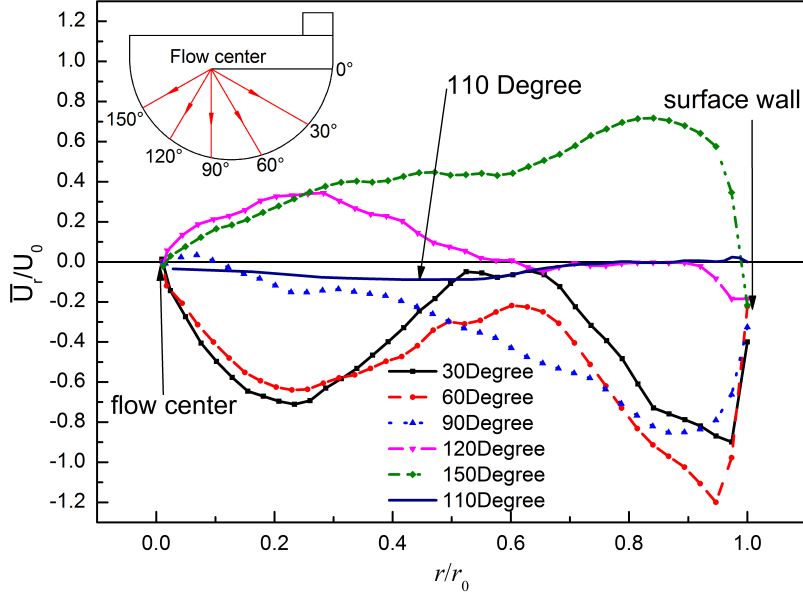
Figure 7: Dependence of the radial velocity U_r on r at different θ as shown in Section 1 for $Re = 10,000$.

but weakly helical. With increasing Re, the overall velocity in the vortex chamber increases. Cases of Re=5,000 display very similar *in-plane* streamline patterns, e.g. a large 'in-plane' vortex is observed close to nozzle 1 and a vortex pair near nozzle 2. As Re increases to 20,000, these vortices disappear. Instead, a large vortex downstream of nozzles is observed. It is found that $Re = 5,000$ and 10,000 cases have a similar streamline distribution while $Re = 20,000$ case is very different. In case $Re = 5,000$ and 10,000, section 4 nearly cuts through the vortex core and cores in cross sections distribute at both sides to section 4. However, as inlet velocity increase, a tiny shift of the entire structure caused by the asymmetric momentum input could cause a relative shift of the measurement location. In the shifted measurement plane, the flow centers are shifted to the nozzle side, and therefore the opposite streamline direction at section 1, $Re = 20,000$.

4.2. Fluctuating velocity

Fig. 9 shows the root-mean-square (rms) value of the velocity v_{rms} calculated by Eq. 7, which quantifies the velocity fluctuation intensity.

$$v_{\text{rms,i,j}} = \sqrt{\frac{\sum_{n=1}^{N}\left(U_{i,j}^{n} - \overline{U_{i,j}}\right)^2}{N} + \frac{\sum_{n=1}^{N}\left(V_{i,j}^{n} - \overline{V_{i,j}}\right)^2}{N}}, i = 1,2,\cdots,160; j = 1,2,\cdots,128 \tag{7}$$

where U, V are fluctuating velocity components, symbol overbar means the average value. $\overline{UV}$ is the Reynolds shear stress and $\overline{UU}$ is the Reynolds normal stress. N is 500. In Section 1, the highest velocity rms is distributed along the interface between the jet and the vortex flow in the chamber, as well as around the vortex core, c.f. Fig. 3. High shear force generated by the core vortex and the jetting vortex at different velocity levels also contributes to the high velocity fluctuation intensity.
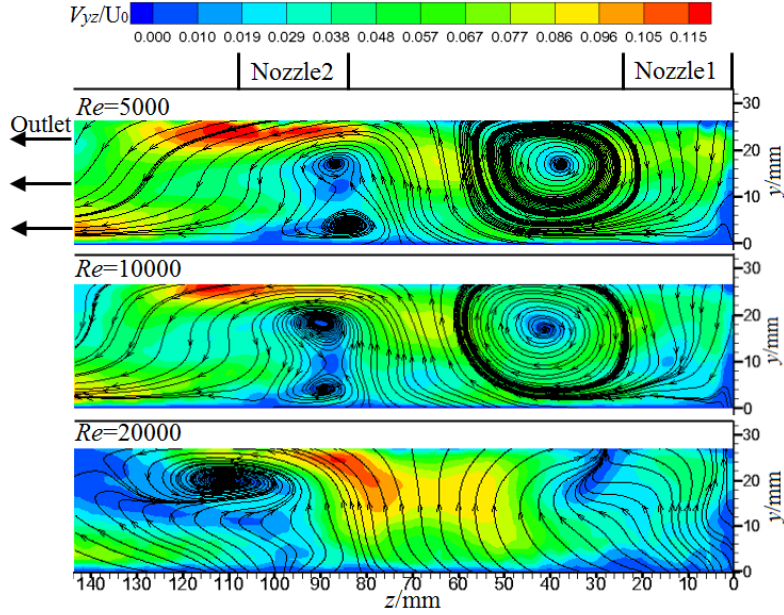
11

Figure 8: Averaged velocity magnitude contour with in-plane streamlines in the longitudinal Section 4.

The shear layer between the main vortex and the corner vortex also creates a high velocity rms. As Re increases, the local velocity fluctuation intensity and the area of high v_{rms}/U_0 increase. The velocity rms distribution over Section 2 has a similar pattern as that in Section 1, except the absent large magnitude around the vortex centre. In Section 3, the overall velocity rms is much lower, but similar to Section 1, a relatively large velocity fluctuation is observed at the vortex centre and the jet-vortex interface. The velocity rms is high at the vortex cneter although the absolute velocity is relatively small. It is mainly because the in-plane vortex at Section 1 is highly unstable which is reflected by the instantaneous vortex center locations. It is found the vortex center moves around (not shown in the paper), which induces high velocity fluctuations. Besides, Section 1 is very closed to the flat end wall, see Fig 2. The complex interaction of the boundary layer developed on this end wall and the strongly rotating inflow is likely to contribute to the vortex instability seen in Section 1. This is likely to be the main reason why high velocity fluctuation is not seen in the vortex core area in Section 2 and 3.

Velocity rms along the centre of the jetting vortex layer, i.e. $r = 23$mm is further investigated in Fig. 10. As Re increases, velocity rms of each section increases as well. For each Re, the fluctuation level at section 1 and 2 is slightly higher than section 3, which is not surprising owing to the jet input. However, the distribution of v_{rms} along $r = 23$mm is section dependent. In Section 1 and 2 with jet input, v_{rms} increases first and then decreases, reaching a peak value at $\theta = 70°$ or so. On the contrary, v_{rms} at section 3 decreases first and then increases along the flow direction. Besides, high v_{rms} is noticed at the start and end at section 3. For the start region, the corner vortex at $0 < x < 10, 25 < y < 34$ influences the flow turbulence, causing a large v_{rms}. In terms of high v_{rms} at the end, we think it is mainly due to the geometrical corner at $50 < x < 54, 28 < y < 34$. The strong turning of the flow direction at the corner might induce significant flow instability and a corner vortex due to the boundary layer effect. This corner vortex is much smaller than the one at the jet inlet and was not resolved by the current PIV resolution. This gives rise to a large v_{rms}.

Fig. 11 presents v_{rms}/U_0 in the longitudinal section. Although the mean velocity magnitude in this section is signifi-
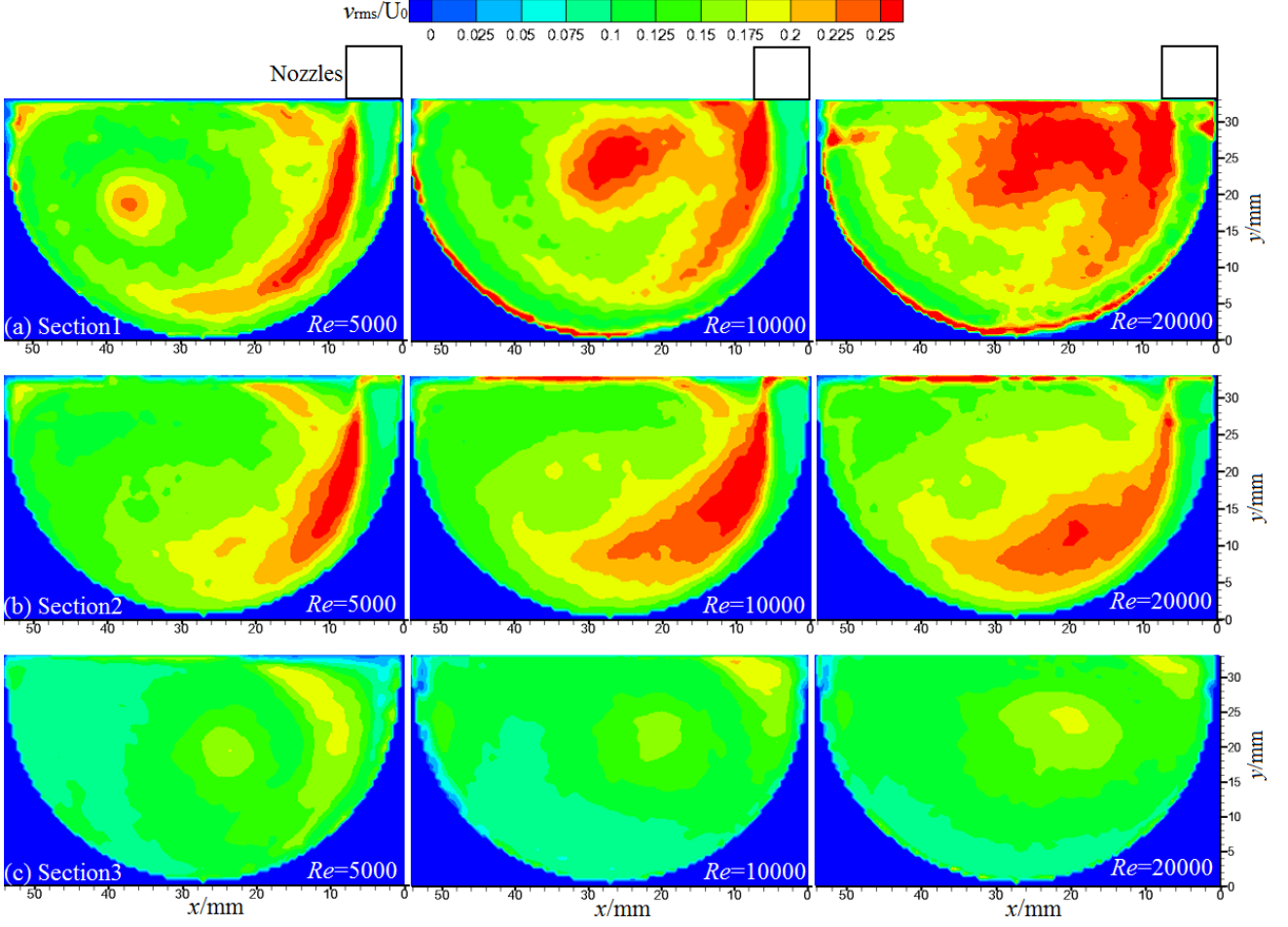
12

Figure 9: Velocity RMS v_{rms} normalised by U_0 in the 3 cross sections.

cantly lower than the cross section (c.f. Fig. 3 and 8), the highest fluctuation intensity is similar and the high intensity area increases with Re. In this particular plane, the largest velocity fluctuation appears to be in between the two nozzles and close to Nozzle 1. The influence of Nozzle 2 increases with Re.

In order to understand the origin of the turbulence fluctuation energy, turbulence production E_{tk} defined in Eq. 8 is further investigated. Considering the average velocity components in x and y direction is almost 10 times larger than that in z direction. The mean velocity distribution also suggests that the velocity gradient is also much larger in the x-y plans for most of the areas. Therefore, it is reasonable to expect that other incomputable production terms related to $\overline{W}$ have relatively small contribution.

$$E_{tk} = -\overline{uv}\frac{\partial \overline{U}}{\partial y} - \overline{u^2}\frac{\partial \overline{U}}{\partial x} - \overline{vu}\frac{\partial \overline{V}}{\partial x} - \overline{v^2}\frac{\partial \overline{V}}{\partial y}, \tag{8}$$

where u, v are fluctuating velocity components, symbol overbar means the average value. $\overline{uv}$ is the Reynolds shear stress and $\overline{uu}$ is the Reynolds normal stress. $\overline{U}$, $\overline{V}$ are average velocity components. E_{tk} reflects how and where the energy is transferred from the mean flow to the turbulent flow. Eq. 8 includes only the computable terms in the cross sectional planes. Even though the fluctuation intensity in the longitudinal plane is similar to that in the cross-sectional planes, the mean flow is only 10% of the latter. Therefore the contribution of the uncomputable terms are believed to be insignificant.
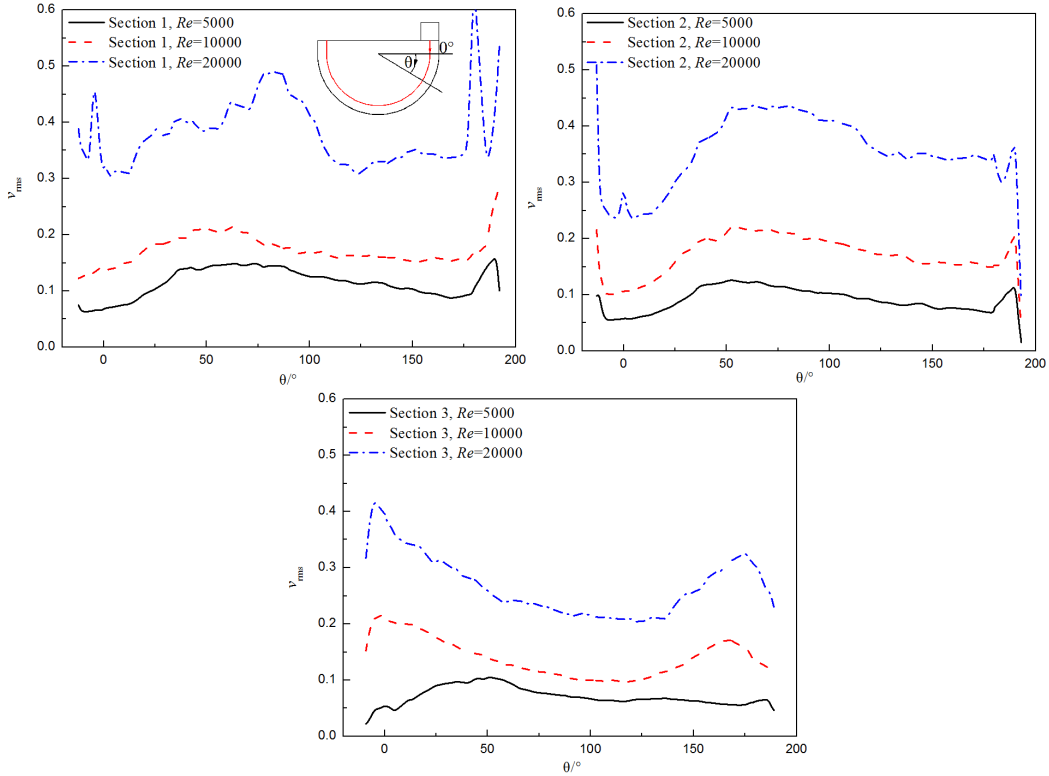
13

Figure 10: v_{rms} along the surface wall of the three cross sections at $r = 23$mm.

E_{tk} contours along with the four terms in Eq. 8 of 3 cross sections at Re=5,000 are presented in Fig. 12. E_{tk} is normalised with U_0^3/L, where L(200mm) is the longitudinal length of the vortex flow chamber. For all cross sections, large E_{tk} is observed near the corner vortex location in the vicinity of the jet input nozzles. For Section 1 and 2, the normal component $(-\overline{u^2}\frac{\partial U}{\partial x})$ and the shear component $(-\overline{vu}\frac{\partial V}{\partial x})$ appear to contribute most to the overall production E_{tk}. The other two terms with negative values tends to balance these two main contributors. The overall E_{tk} in Section 3 is smaller than others not surprisingly due to the low velocity level, and the normal component $(-\overline{u^2}\frac{\partial U}{\partial x})$ has the dominant contribution. The overall E_{tk} distribution suggests that the velocity gradient along the horizontal x direction is most responsible to generate velocity fluctuations. Turbulence is mainly generated near the corner vortex at the jet inlet and then extends to the downstream in line with Fig. 9. Another area of high E_{tk} is in the boundary layer along the cylindrical wall. For this outermost layer, data has a sudden change from zero (the outer region is set zero). The differential terms would have a much larger value on this layer, causing unusual blue or red stripes. This meaningless layer shouldn't be taken into consideration when discussing.

4.3. POD analysis

In this section, POD was applied to extract energetic coherent flow motions from an ensemble of 500 statistically independent snapshots. The ranked modal energy content of the first 20 modes is presented in Fig. 13. Mode 0 refers to the mean flow field which has been discussed in §4.1. The modal energy distribution becomes more or less Re and section independent for $n > 10$. Taking the case of Section 1, Re=10,000 as an example, at the fifth mode, the modal energy contribution decreases to about 2% approximately (the first 5 modes: 10.5%, 5.4%, 4.2%, 3.1%, 2.4% respectively). The total contribution of the first 4 modes is about 23.2%, which contain most important structures of the flow. Thus these 4
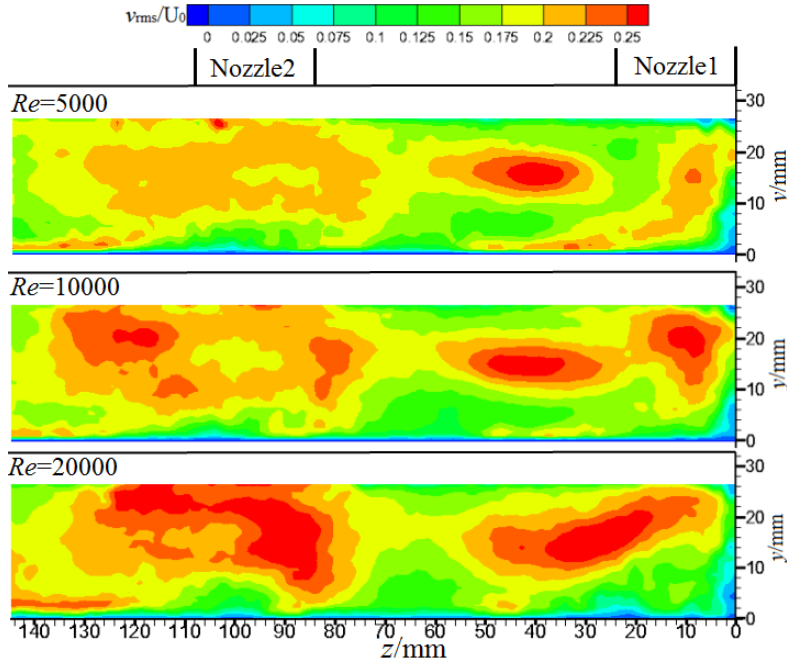
14

Figure 11: Distribution of the velocity rms $v_{\mathrm{rms}}/\mathrm{U}_0$ in the longitudinal section.

eigenmode distributions are investigated over Section 1.

Fig.14 shows the spatial pattern of the first 4 eigenmodes, with streamlines superimposed on the normalized vorticity contour. The vorticity ω is calculated as $\partial V/\partial x - \partial U/\partial y$, and ω_0 is set as 0.001 for the purpose of normalization for section 1. Nozzle 1 is positioned at the same location as Fig. 3. Comparing $Re = 5,000$ case with the other higher Re cases, the flow pattern in the first 2 modes is swapped. That is, mode 1 at Re=5,000 shows a strong vortex near the surface wall at $0 < x < 30$ mm and $0 < y < 25$ mm approximately. The induced velocity would strengthen the shear on the local boundary layer, resulting in enhanced heat exchange between the coolant and surface wall. High vorticity region is also observed at the jet exit, with the opposite signs associated with the two shear layers of the jet. The shear layer with the positive vorticity also interacts with the vortex just mentioned. These features are observed in Mode 2 of $Re = 10,000$ and $20,000$ cases.

A distinctive feature of Mode 2 of $Re = 5,000$ case is a clockwise and a counterclockwise vortex pair at the core area of the mean flow vortex; cf Fig. 3. Similar characteristics is seen in Mode 1 of the other two Re cases, although the counterclockwise rotating vortex is not pronounced. It may be speculated by the eigenmode distribution of seciton 1 in Fig. 13 that λ_1 at Re=10,000 is much larger than Re=5,000, which is not significantly higher than λ_2 of Re=10,000. It suggests that the high energetic jet in $Re = 10,000$ and $20,000$ is able to transfer its energy to the core vortex more effectively than $Re = 5,000$. It further suggests a Re threshold at which the strength of the vortex along the wall boundary (induced by the jet) is overtaken by the core vortex.

For mode 3 and mode 4, the main patterns are the core vortex, near-wall vortex and vortices due to their interaction. As Re increases to 20,000, the flow pattern of different modes is similar to Re=10,000, and the number of small vortices has a further reduction.

For Mode 3 and 4, vortices appear to be smaller and incoherent, which tend to distributed along the cylindrical wall. As Re increases, these small vortices appear reduced in number. It suggests that the flow near the wall is highly complex
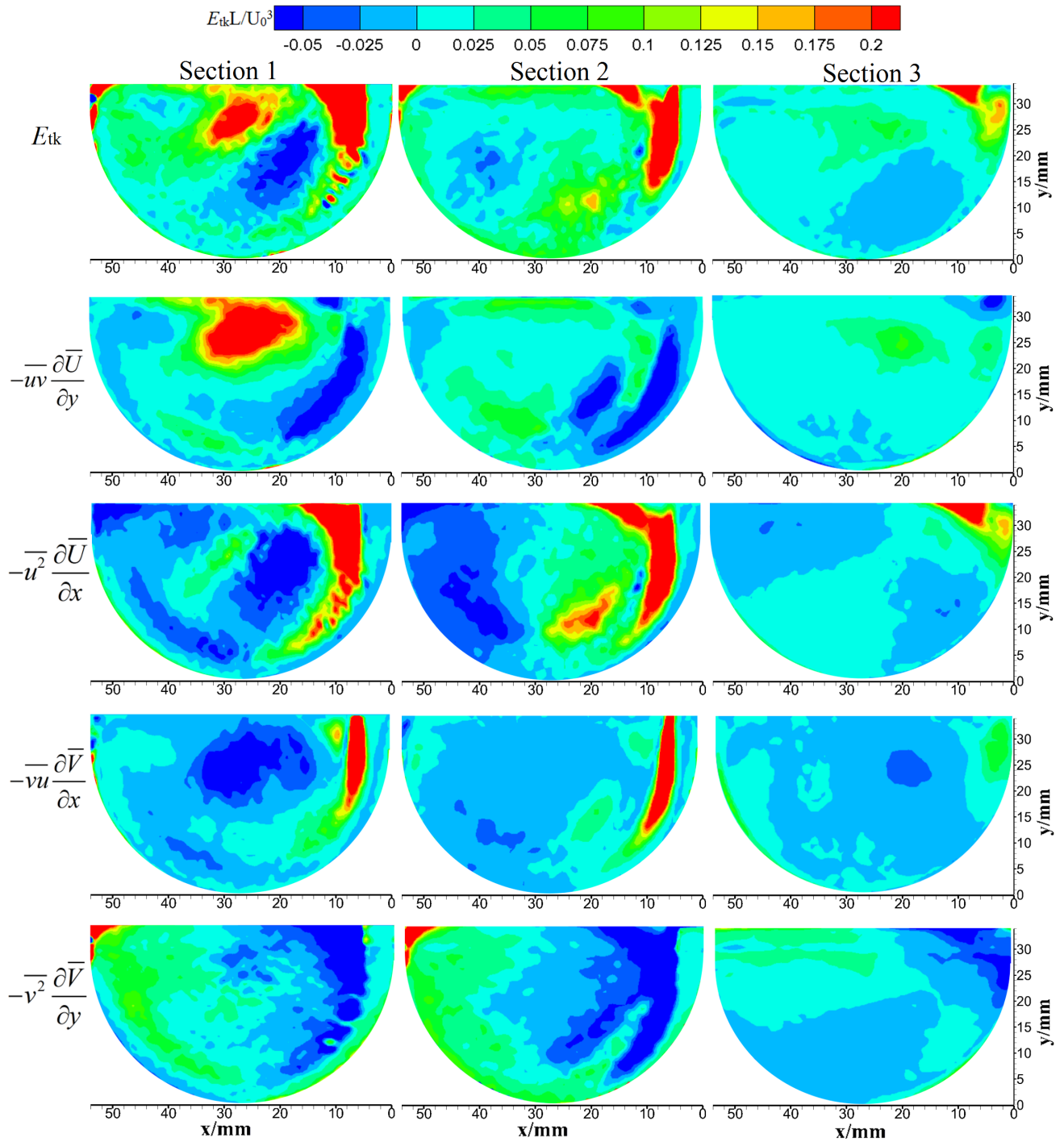
15

Figure 12: Contours of turbulence production E_{tk} and its four terms in the cross sections at Re=10,000. E_{tk} is normalised by U_0^3/L
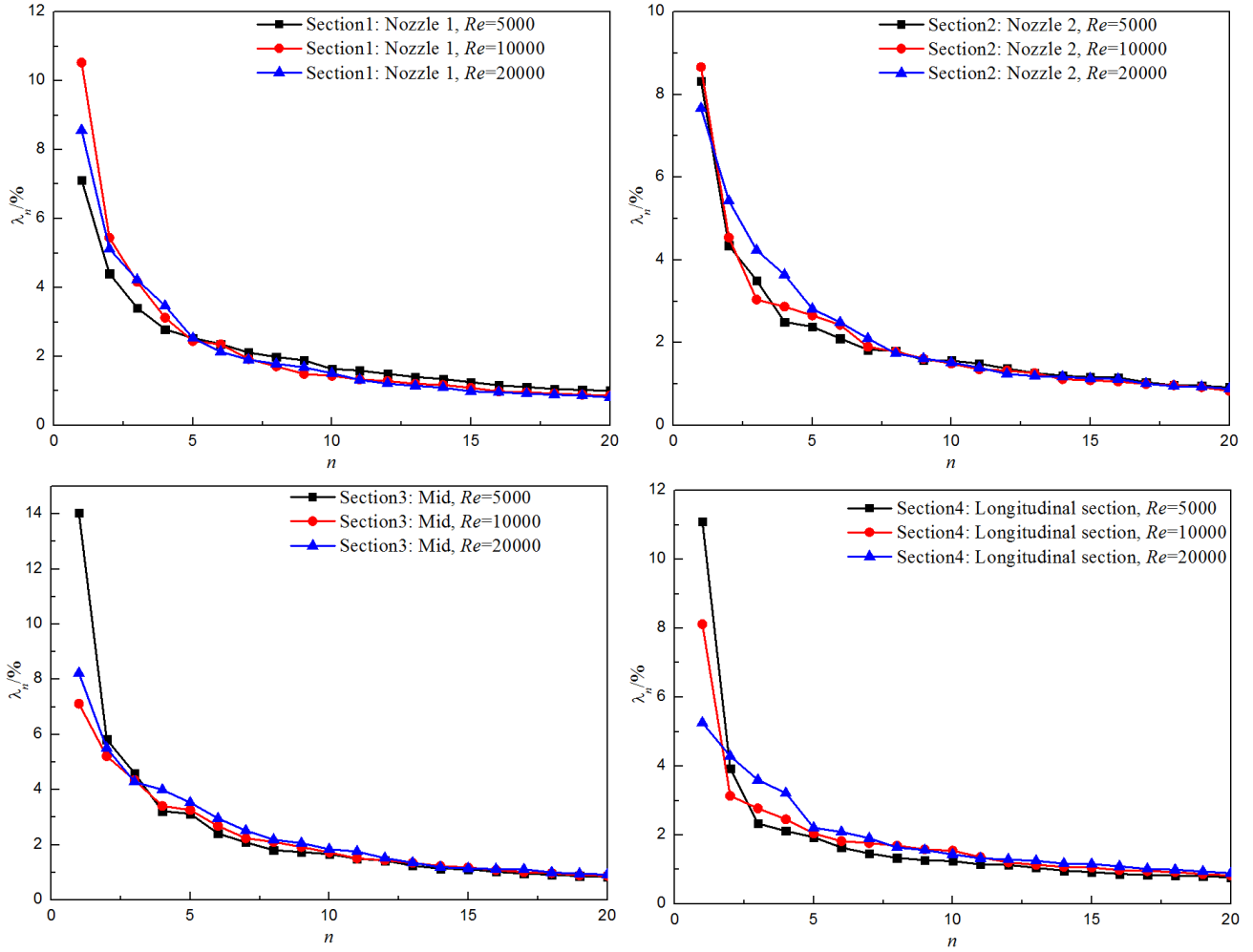
Figure 13: Normalized eigenvalues of the first 20 eigenmodes.

compared to the central area. In the two higher *Re* cases, the influence of the core vortex remains important in these two modes. As *Re* increases to 20,000, the modes are similar to that in *Re*=10,000, but the number of small incoherent vortices further reduced.

Analysis of these modes allows us to examine the energy content in different flow structures. In particular, it indicates that for the current vortex cooling configuration, the high turbulence level in the core area in Fig. 9 is contributed by the dominant vortex with energy content of $4.2\%, 10.5\%, 8.7\%$ for the three *Re* cases respectively. This energy of the vortex core is reflected in higher eigenmodes. The large turbulence intensity along the wall is contributed by a coherent vortex near the boundary induced by the jet as well as those incoherent vortices only pronounced at mode 3 and higher. These flow structures carry $4.3\%, 5.5\%, 5\%$ of the total fluctuation energy, respectively.

The first 4 most energetic modes in Section 3 are also presented in Fig. 15. Different from Section 1, the dominant vortex structure in this section is the vortex pair in the central area of the chamber. No coherent vortex near the surface wall can be seen, as there is no direct jet input in this section. However, perhaps due to the effect of the strong cross flow, major fluctuating energy tends to locate at the right corner; see Fig. 9, which is also consistent to the corner vortex observed in Fig. 3c. As *Re* increases, the effect of the cross flow seems to get stronger, resulting in more intensified fluctuating energy
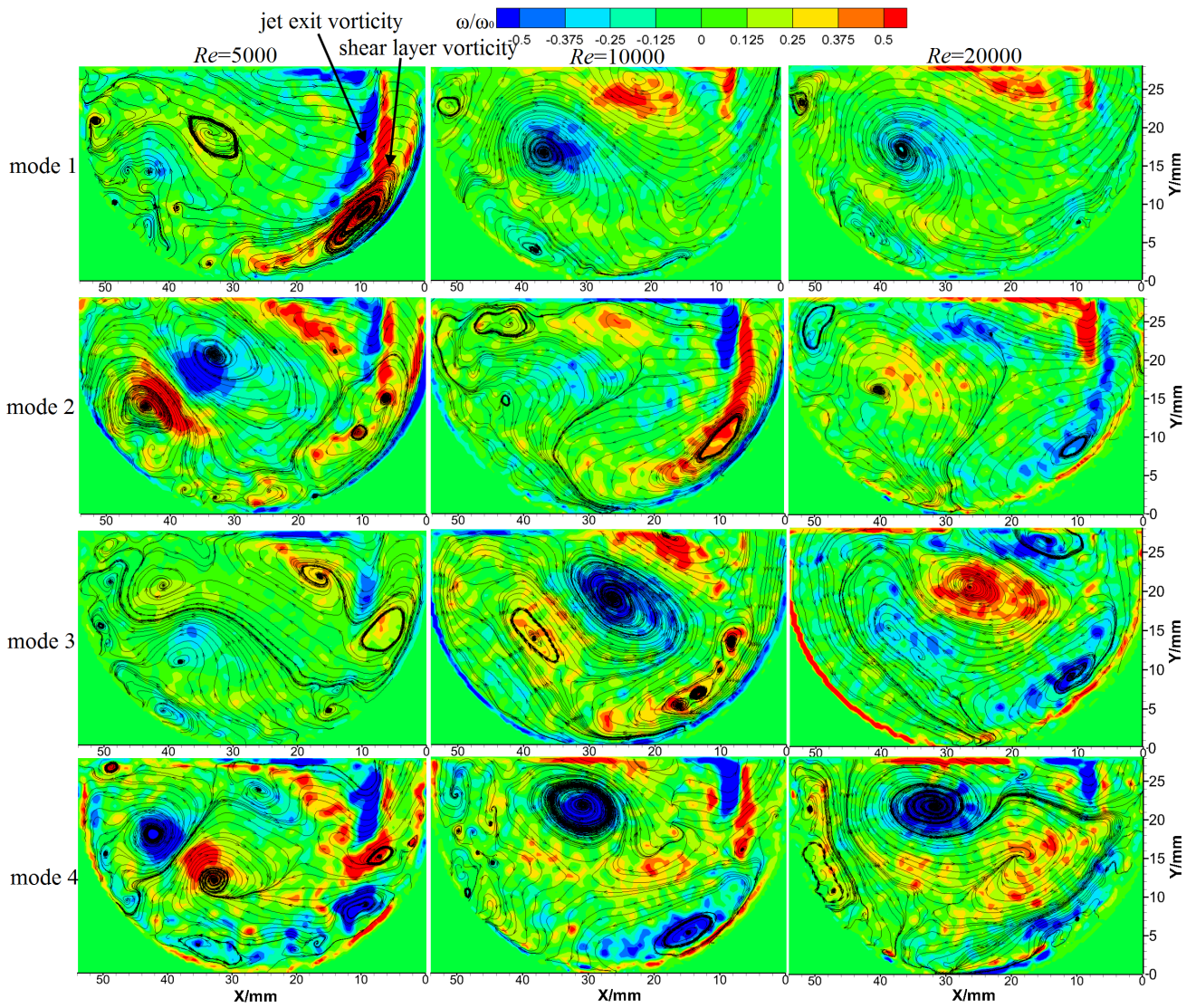
17

Figure 14: First 4 eigenmodes of the flow field in Section 1.

at the upper right corner. In Fig. 6, the heat transfer at the region between nozzles presents a decreasing distribution along the circumferential flow direction. Besides, a local high Nusselt number region is observed near nozzles. In terms of the vorticity, the distribution is consistent to the vortices.
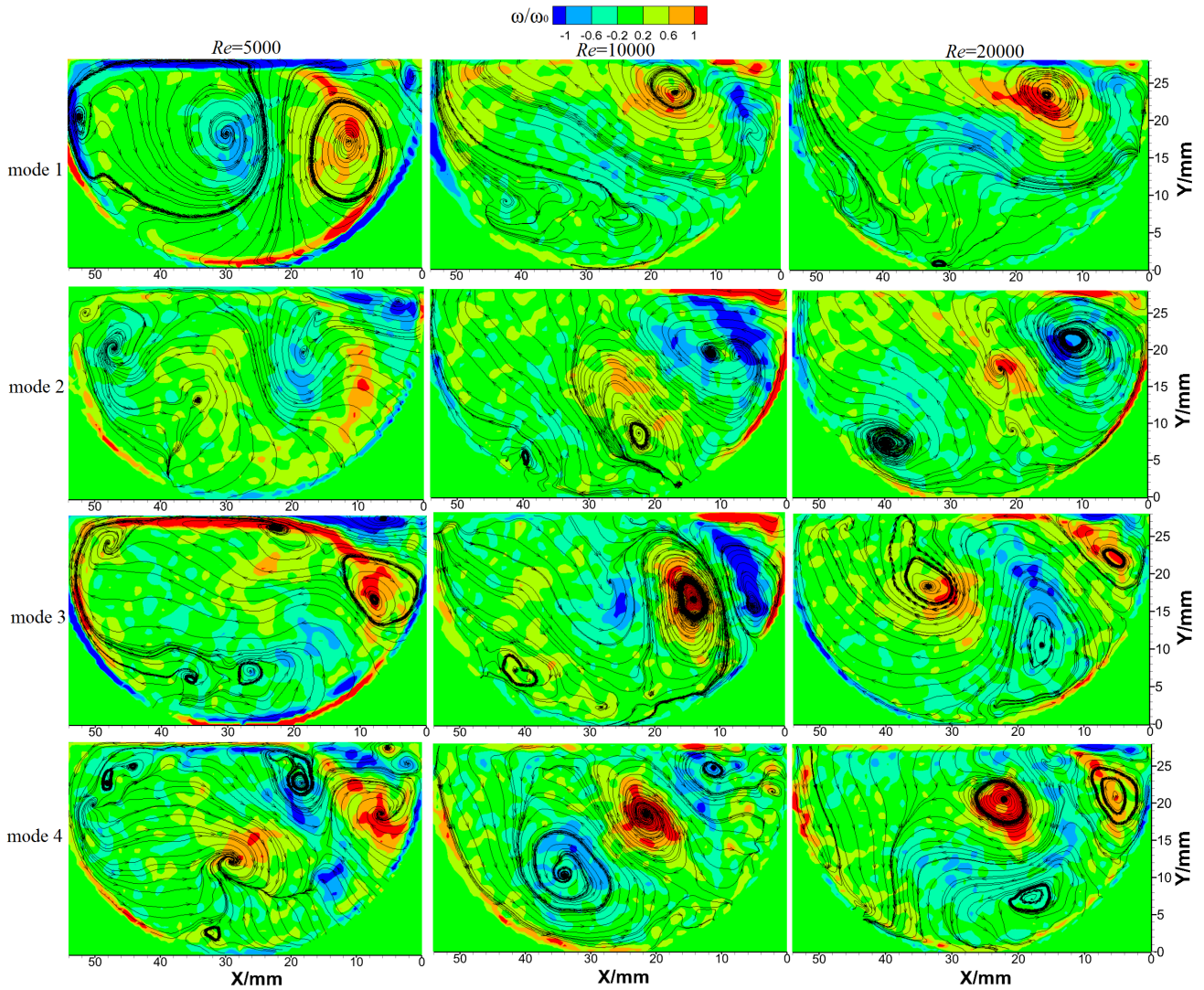

Figure 15: First 4 modes of the flow field of Section 3.

5. Conclusion

In this paper, planar PIV was conducted to investigate the vortex flow characteristics in a semi cylinder vortex cooling model with 2 inlets jets. The flow fields as well as the fluctuating velocity at 3 cross sections and a longitudinal section along the cylinder axis at 3 Re were studied. In addition, snapshot based POD was used to extract coherent flow structures.

The tangential jet inflow forms a large-scale vortex in the chamber with a small recirculating corner vortex near the jet inlet. The core vortex is similar to a Rankine vortex with a core solid body rotating vortex, surrounded by a jetting vortex layer and then a boundary layer at the chamber wall, although the vortex is highly distorted due to the semi cylindrical chamber. The jetting vortex layer is mainly responsible for heat transfer enhancement. Considering the velocity magnitude

19

in the axial direction is about 10% of that in the cross sections, the 3D flow is supposed to be strongly rotational with a weak helical nature.

For nozzle sections having jet inflow (Section 1 and 2), the circumferential velocity along the jetting vortex layer has a turning region at $\theta \approx 170°$. Before that the circumferential flow remains energetic, while after that the circumferential velocity has a very large decay rate. This flow characteristic provides a flow dynamic explanation to the observed heat transfer intensity in a similar configuration. Especially for the cross section adjacent to the side wall at Re=10,000 and 20,000, velocity has a slight increase until $\theta \approx 110°$. In terms of the radial velocity along the radial distances, for $\theta < 110°$ it points to the chamber central region which is beneficial to take hot fluid from the outer wall. Contrarily, for $\theta > 110°$ the mean flow has a weak outward velocity, weakening the heat transfer effect.

In cross sections, the interface between the jet and the vortex flow has the largest fluctuating velocity intensity and this is also where turbulence is produced from the energy in the mean flow. As Reynolds number increases, both the intensity and the area of the fluctuation increase. Velocity rms along the circumferential flow direction increases first and then decreases, while the fluctuation in between the cross sections with jet inflow shows an opposite distribution. For the longitudinal section, the mean velocity is low compared to cross sections, but the fluctuating velocity intensity has a comparative level.

POD analysis reveals that the large-scale vortex near the surface wall has the dominant contribution to the fluctuation energy, while in the section in between the jet inflow, the coherent flow structure consists of a vortex pair in the core and a corner vortex. In the cross section adjacent to the chamber sidewall, the energetic jet transfers its energy more effectively and a Re threshold at which the strength of the vortex along the wall boundary is overtaken by the core vortex.

List of symbols

D	Main pipe diameter
M	Number of grid data points
N	Total number of vector fields
Nu	Nusselt number
Re	Inlet Reynolds number based on tube diameter
r	Radial length
r_0	Radius of the vortex chamber
U	Instantaneous velocity in the X direction
$\overline{U}$	Average velocity in the X direction of 500 images
$\overline{u}$	Average fluctuating velocity in the X direction of 500 images
U_0	Coolant velocity through nozzles
$\overline{U}_\theta$	Azimuthal velocity
$\overline{U}_r$	Radial velocity
V	Instantaneous velocity in the Y direction
$\overline{V}$	Average velocity in the Y direction of 500 images
$\overline{v}$	Average fluctuating velocity in the Y direction of 500 images
V_0	Inflow velocity
V_{xy}	Velocity defined as $\sqrt{\overline{U}^2 + \overline{V}^2}$
V_{yz}	Velocity defined as $\sqrt{\overline{V}^2 + \overline{W}^2}$
v_{rms}	Fluctuating velocity
$\overline{W}$	Average velocity in the Z direction of 500 images
ω	Vorticity defined as $\partial V/\partial x - \partial U/\partial y$
θ	Circumferential angle
λ_n	Relative contribution of the eigenmodes to the total fluctuation energy at mode n
ρ	Water density
μ	Water dynamic viscosity

Abbriviations

MRV	Magnetic Resonance Velocimetry
PIV	Paticle Image Velocimetry
POD	Proper Orthogonal Decomposition
PTV	Particle Tracking Velocimetry
RANS	Reynolds Average Navier-stokes

Acknowledgement

References

References

[1] Y. Xu, Y. Zhang, F. C. G. A. Nicolleau, Z. Wang, Piv of swirling flow in a conical pipe with vibrating wall, International Journal of Applied Mechanics 10 (2018).

[2] N. Hay, P. D. West, Heat transfer in free swirling flow in a pipe, Journal of Heat Transfer 97 (1975) 411–416.

[3] J. C. Han, S. Dutta, Recent developments in turbine blade internal cooling, Ann N Y Acad Sci 934 (2001) 162–178.

[4] F. Kreith, D. Margolis, Heat transfer and friction in turbulent vortex flow, Applied Scientific Research 8 (1959) 457–473.

[5] F. Kreith, O. K. Sonju, The decay of a turbulent swirl in a pipe, Journal of Fluid Mechanics 22 (1965) 257–271.

[6] X. Fan, L. Li, J. Zou, Y. Zhou, Cooling methods for gas turbine blade leading edge: Comparative study on impingement cooling, vortex cooling and double vortex cooling, International Communications in Heat and Mass Transfer 100 (2019) 133–145.

[7] P. M. Ligrani, T. Blaskovich, M. M. Oliveira, Comparison of heat transfer augmentation techniques, Aiaa Journal 41 (2003) 337–362.

[8] B. Glezer, H.-K. Moon, T. O'Connell, A novel technique for the internal blade cooling, in: ASME 1996 International Gas Turbine and Aeroengine Congress and Exhibition, American Society of Mechanical Engineers, 1996, pp. V004T09A015–V004T09A015.

[9] C. Hedlund, P. Ligrani, H.-K. Moon, B. Glezer, Heat transfer and flow phenomena in a swirl chamber simulating turbine blade internal cooling, in: ASME 1998 International Gas Turbine and Aeroengine Congress and Exhibition, American Society of Mechanical Engineers, 1998, pp. V004T09A081–V004T09A081.

[10] C. Hedlund, P. Ligrani, B. Glezer, H.-K. Moon, Heat transfer in a swirl chamber at different temperature ratios and reynolds numbers, International journal of heat and mass transfer 42 (1999) 4081–4091.

[11] C. R. Hedlund, P. Ligrani, Local swirl chamber heat transfer and flow structure at different reynolds numbers, Journal of turbomachinery 122 (2000) 375–385.

[12] J. P. Ling, P. T. Ireland, N. W. Harvey, Measurement of heat transfer coefficient distributions and flow field in a model of a turbine blade cooling passage with tangential injection, in: ASME Turbo Expo 2006: Power for Land, Sea, and Air, American Society of Mechanical Engineers, 2006, pp. 325–340.

[13] Z. Liu, J. Li, Z. Feng, Numerical study of swirl cooling in a turbine blade leading-edge model, Journal of Thermophysics and Heat Transfer 29 (2015) 166–178.

[14] Z. Liu, J. Li, Z. Feng, T. Simon, Numerical study on the effect of jet nozzle aspect ratio and jet angle on swirl cooling in a model of a turbine blade leading edge cooling passage, International Journal of Heat and Mass Transfer 90 (2015) 986–1000.

[15] L. Zhao, J. Li, Z. Feng, T. Simon, Numerical study on the effect of jet spacing on the swirl flow and heat transfer in the turbine airfoil leading edge region, Numerical Heat Transfer 70 (2016) 980–994.

[16] C. Du, L. Liang, W. Xin, Z. Feng, Effect of jet nozzle geometry on flow and heat transfer performance of vortex cooling for gas turbine blade leading edge, Applied Thermal Engineering 93 (2016) 1020–1032.

[17] C. Du, L. Liang, X. Fan, Numerical study on vortex cooling flow and heat transfer behavior under rotating conditions, International Journal of Heat and Mass Transfer 105 (2017) 638–647.

[18] C. Du, Effect of jet nozzle geometry on flow and heat transfer performance of vortex cooling for gas turbine blade leading edge, Applied Thermal Engineering 93 (2016) 1020–1032. doi:10.1016/S0031-8914(53)80099-6.

[19] A. H. Nissan, V. P. Bresan, Swirling flow in cylinders, Aiche Journal 7 (1961) 543–547.

[20] M. K. King, R. R. Rothfus, R. I. Kermode, Static pressure and velocity profiles in swirling incompressible tube flow, Aiche Journal 15 (1969) 837–842.

[21] T. Akiyama, M. Ikeda, Fundamental study of the fluid mechanics of swirling pipe flow with air suction, Industrial and Engineering Chemistry Process Design and Development 25 (1986) 907–913.

[22] O. Kitoh, Experimental study of turbulent swirling flow in a straight pipe, Journal of Fluid Mechanics 225 (1991) 445–479. doi:10.1017/S0022112091002124.

[23] H. Li, Y. Tomita, Characteristics of swirling flow in a circular pipe, Journal of Fluids Engineering 116 (1994) 370–373.

[24] A. Gupta, R. Kumar, Three-dimensional turbulent swirling flow in a cylinder: Experiments and computations, International journal of Heat and fluid flow 28 (2007) 249–261.

[25] S. Grundmann, F. Wassermann, R. Lorenz, B. Jung, C. Tropea, Experimental investigation of helical structures in swirling flows, International Journal of Heat and Fluid Flow 37 (2012) 51–63.

[26] J.-C. Han, Turbine blade cooling studies at texas a&m university: 1980-2004, Journal of thermophysics and heat transfer 20 (2006) 161–187.

[27] L. Sirovich, Turbulence and the dynamics of coherent structures. i. coherent structures, Quarterly of applied mathematics 45 (1987) 561–571.

23

[28] L. Graftieaux, M. Michard, N. Grosjean, Combining piv, pod and vortex identification algorithms for the study of unsteady turbulent swirling flows, Measurement Science and technology 12 (2001) 1422.

[29] C. Biegger, B. Weigand, A. Cabitza, Three components-and tomographic-piv measurements of a cyclone cooling flow in a swirl tube, in: ASME Turbo Expo 2013: Turbine Technical Conference and Exposition, American Society of Mechanical Engineers, 2013, pp. V03AT12A012–V03AT12A012.